Monthly Notices
of the
ROYAL ASTRONOMICAL SOCIETY

MNRAS **430,** 1158–1170 (2013) doi:10.1093/mnras/sts684

The merger rates and sizes of galaxies across the peak epoch of star formation from the HiZELS survey

John P. Stott,[1]⋆ David Sobral,[2] Ian Smail,[1] Richard Bower,[1] Philip N. Best[3] and James E. Geach[4]

[1]*Institute for Computational Cosmology, Durham University, South Road, Durham, DH1 3LE, UK*
[2]*Leiden Observatory, Leiden University, PO Box 9513, NL-2300 RA Leiden, the Netherlands*
[3]*SUPA, Institute for Astronomy, Royal Observatory of Edinburgh, Blackford Hill, Edinburgh, EH9 3HJ, UK*
[4]*Department of Physics, McGill University, Ernest Rutherford Building, 3600 Rue University, Montreal, Quebec H3A 2T8, Canada*

Accepted 2012 December 20. Received 2012 December 18; in original form 2012 August 14

ABSTRACT

We use the HiZELS narrow-band Hα survey in combination with CANDELS, UKIDSS and WIRDS near-infrared imaging, to investigate the morphologies, merger rates and sizes of a sample of Hα emitting galaxies in the redshift range $z = 0.40$–2.23, an epoch encompassing the rise to the peak of the star formation rate density. Merger rates are estimated from space- and ground-based imaging using the M_{20} coefficient. To account for the increase in the specific star formation rate (sSFR) of the star forming 'main sequence' with redshift, we normalize the star formation rates of galaxies at each epoch to the typical value derived from the Hα luminosity function. Once this trend in sSFR is removed we see no evidence for an increase in the number density of star-forming galaxies or the merger rate with redshift. We thus conclude that neither is the main driver of the enhanced star-formation rate density at $z \sim 1$–2, with secular processes such as instabilities within efficiently fuelled, gas-rich discs or multiple minor mergers the most likely alternatives. However, we find that ∼40–50 per cent of starburst galaxies, those with enhanced specific star formation at their epoch, are major mergers and this fraction is redshift independent. Finally, we find the surprising result that the typical size of a star-forming galaxy of a given mass does not evolve across the redshift range considered, suggesting a universal size–mass relation. Taken in combination, these results indicate a star-forming galaxy population that is statistically similar in physical size, merger rate and mass over the ∼6 Gyr covered in this study, despite the increase in typical sSFR.

Key words: galaxies: evolution – galaxies: interactions – galaxies: star formation.

1 INTRODUCTION

The peak in the volume averaged star formation rate (SFR) for galaxies occurs in the redshift range $z = 1$–3 (Lilly et al. 1996; Madau et al. 1996; Sobral et al. 2013). At this epoch, the SFR in typical galaxies is of an order of magnitude higher than that in the local Universe (Reddy & Steidel 2009). This is the era when most of the stars in the Universe were formed and represents the peak in black hole activity. The task is now to address 'how' and 'why' the Universe was so different then.

A picture is emerging in which the dominant mode of star formation at this earlier epoch is very different to that in the local Universe. Rather than the quiescent formation of stars that is the norm in today's Universe, violent episodes of star formation are dominated by the formation of superstar clusters (e.g. Swinbank et al. 2010b). However, the origin of these differences is somewhat controversial: one picture, which has some observational support, is that they are driven by an increase in the galaxy merger rate (e.g. Somerville, Primack & Faber 2001; Conselice et al. 2003; Hopkins et al. 2006; Conselice, Rajgor & Myers 2008), but other theories have suggested that it is the result of the higher rate of gas accretion expected in the high-redshift Universe (Kereš et al. 2005; Dekel, Sari & Ceverino 2009). It is therefore important to study the SFR, merger fractions and gas content of these galaxies in order to identify the processes responsible for driving this epoch of enhanced activity.

In recent years, the presence of a star forming 'main sequence' seen in the local Universe (e.g. Brinchmann et al. 2004) has been confirmed at increasingly high redshift (Daddi et al. 2007; Elbaz et al. 2007, 2011; Rodighiero et al. 2011; Sargent et al. 2012). This is a relation between SFR and stellar mass for star-forming galaxies, with a typical specific star formation rate (sSFR, the ratio of the SFR to the stellar mass of the galaxy) found to increase with

⋆E-mail: j.p.stott@durham.ac.uk

redshift (Elbaz et al. 2011). Galaxies that lie off this relation with sSFRs too high to be in the typical star-forming population are often described as 'starbursts' and are thought to be triggered by violent events such as major mergers (Hopkins et al. 2006; Elbaz et al. 2007; Rodighiero et al. 2011).

From a theoretical perspective, in the Λ cold dark matter (ΛCDM) paradigm dark matter haloes merge hierarchically from the bottom up, with the largest haloes created at later times (e.g. Lacey & Cole 1993; Cole et al. 2000; Springel et al. 2005). As the galaxies trace the underlying dark matter we therefore expect those to merge hierarchically also. However, it has been known for sometime that the most massive galaxies appear to have older stellar populations than their less massive counterparts (Cowie et al. 1996; Bower et al. 2006; Gilbank et al. 2010). Environment also plays a key role with massive quiescent galaxies typically living in denser environments than lower mass star-forming galaxies (Dressler 1980). There are several ways to reconcile these observations with hierarchical merging which are implemented in phenomenological, semi-analytic models that seek to reproduce observations of galaxy evolution by populating dark matter haloes from *N*-body simulations with mock galaxies (e.g. Bower et al. 2006; Croton et al. 2006). A reasonable match is achieved through interactions and feedback mechanisms that cease star formation in massive galaxies within massive dark matter haloes, requiring that these galaxies build up their stellar mass at late times by so-called dry mergers which trigger no significant new star formation due to the lack of available cold gas (De Lucia & Blaizot 2007).

In the high-redshift Universe the cold gas fraction in galaxies is higher than at low redshift and thus there is more fuel for star formation (e.g. Tacconi et al. 2010; Geach et al. 2011). It is therefore possible to more easily trigger significant star-forming events during mergers (Somerville et al. 2001) or through high gas accretion rates and disc instabilities in isolated galaxies (Kereš et al. 2005; Bower et al. 2006; Dekel et al. 2009; Förster Schreiber et al. 2011; Cacciato, Dekel & Genel 2012). The latter process leads to the intriguing possibility of the enhanced SFRs at high redshift being dominated by secular evolution rather than mergers. In fact, while some observations suggest an increase in the merger fraction with redshift (Conselice et al. 2003) others seem to prefer in situ galactic processes over galaxy–galaxy merging, or at least a mixture of these processes (Elbaz et al. 2007; Lotz et al. 2008).

To test whether it is galaxy mergers or secular processes that dominate and drive galaxy evolution at the peak era for star formation, a method to distinguish between galaxy mergers and non-mergers needs to be implemented. The two main methods of estimating the merger fraction are counting close pairs of galaxies, under the assumption that they will subsequently merge (e.g. Le Fèvre et al. 2000; Lin et al. 2008; Bluck et al. 2009), and using a method of identifying galaxies with a merging morphology (e.g. Conselice et al. 2003, 2008; Lotz, Primack & Madau 2004; Lotz et al. 2008; Conselice, Yang & Bluck 2009). The results of both of these methods often suggest that the merger fraction increases with redshift and, depending on the mass range considered, the merger fraction at $z \gtrsim 1$, where the star formation rate density (SFRD) peaks, is roughly $\sim$0.1–0.3 on average (but with some systematic offsets between studies) compared to a fraction $\lesssim$0.1 in the local Universe. A third, potentially more reliable, method is to employ detailed integrated field unit observations of $z = 1$–2 galaxies to look for merger signatures in the dynamics of the galaxies. Such studies, although generally smaller in sample size, also find a merger fraction of $\sim$0.3 (e.g. Shapiro et al. 2008; Förster Schreiber et al. 2009).

In order to study the star-forming population, an excellent tracer of ongoing star formation is the Hα emission line which is less affected by dust obscuration than shorter wavelength star formation tracers [e.g. ultraviolet (UV) continuum light or [O II]3727]. Unfortunately beyond $z = 0.4$, Hα is redshifted out of the optical window; thus, high-redshift studies of star formation have been limited to either using the obscuration-effected short wavelength tracers or studying small samples of Hα emitters using conventional near-infrared spectrographs. However, in the last few years panoramic narrow-band surveys have started to provide large samples of Hα-selected galaxies [e.g. the High-redshift (Z) Emission Line Survey (HiZELS); Geach et al. 2008, 2012; Sobral et al. 2009, 2010, 2012, 2013; Garn et al. 2010 and the studies of Villar et al. 2008; Ly et al. 2011]. Narrow-band surveys provide a well-understood, volume-selected sample of star-forming galaxies allowing for straightforward analysis of trends with SFR, mass and size etc. They provide emission line information over large areas of the sky and are thus able to probe a significant range of the Hα luminosity and stellar mass functions for star-forming galaxies, required for an unbiased analysis of the SFRD (e.g. Geach et al. 2008; Sobral et al. 2009, 2012, 2013). This selection method has also been shown to be extremely effective at detecting intrinsically faint galaxies, helping to overcome the bias towards massive galaxies associated with photometric redshift selection.

In this study, we use the $z = 0.4$–2.23 HiZELS sample presented in (Sobral et al. 2013), to not only analyse the merger rate as a function of redshift and stellar mass but also as a function of the well-determined SFR. We can therefore test whether it is major mergers that drive the rise to enhanced activity seen at these epochs. In contrast to earlier studies, which analyse *Hubble Space Telescope* (*HST*) rest-frame UV morphologies, with the advent of the Wide Field Camera 3 (WFC3) camera we can also study the rest-frame optical bands for a subsample of our galaxies that lie within the Cosmic Assembly Near-infrared Deep Extragalactic Legacy Survey (CANDELS) region of our survey and use this to calibrate morphologies derived from deep, wide-field, ground-based near-infrared imaging, better matched to the extent of the full HiZELS fields. We also analyse the size–mass relation for star-forming galaxies over this epoch in order to study the size evolution, which may also indicate the merger history of these systems.

The structure of this paper is as follows. In Section 2, we describe the HiZELS narrow-band sample and the imaging data. We then derive SFR for the sample and analyse the evolution of the number density of galaxies above a given SFR. The size–mass relation is then studied in order to look for an evolution. A method for automating morphological classification is defined and this is used to study the merger rates of the galaxies in our sample and how they evolve and depend on SFR and mass. Finally, we discuss our findings in the context of understanding the physical processes that occur within galaxies, that lead to the rapid downturn in the global volume averaged SFR below $z \sim 1$.

A ΛCDM cosmology ($\Omega_{\rm m} = 0.27$, $\Omega_\Lambda = 0.73$, $H_0 = 70$ km s^{-1} Mpc^{-1}) is used throughout this work and all magnitudes are AB.

2 THE SAMPLE AND DATA

2.1 The HiZELS survey

HiZELS (Geach et al. 2008; Sobral et al. 2013) is a campaign project using the Wide Field CAMera (WFCAM; Casali et al. 2007) on the United Kingdom Infrared Telescope (UKIRT) and exploits

specially designed narrow-band filters in the J and H bands (NBJ and NBH), along with the H_2S1 filter in the K band, to undertake panoramic, moderate depth surveys for line emitters. HiZELS targets the Hα emission line redshifted into the near-infrared at $z = 0.84$, 1.47 and 2.23 using these filters. In addition, the UKIRT data are complemented by deeper narrow-band observations with Subaru Suprime-Cam NB921 imaging (Sobral et al. 2012, 2013) to obtain Hα emitting galaxies at $z = 0.4$ and the [O II] emission from the $z = 1.47$ Hα sample, as well as deeper WFCAM and Very Large Telescope near-infrared imaging through the H_2S1 filter in selected fields. The survey is designed to trace star formation activity across the likely peak of SFRD and provide detailed information about a well-defined statistical sample of star-forming galaxies at each epoch (see Best et al. 2010).

In this study, we concentrate on the main HiZELS sample of $z = 0.4$, 0.84, 1.47 and 2.23 Hα emitters in both the UKIRT Infrared Deep Sky Survey, Ultra Deep Survey (UKIDSS UDS; Lawrence et al. 2007; Almaini et al., in preparation) and the Cosmic Evolution Survey (COSMOS; Scoville et al. 2007) fields as described in Sobral et al. (2013) and we refer the reader to that paper for full details of the catalogues used. These data cover areas of 0.6–1.6 square degrees depending on the field and waveband. The narrow-band excess sources are visually inspected to remove image artefacts and, to ensure the galaxies are at the desired redshift, spectral energy distribution (SED) fitting and optimized colour–colour selections are used to provide clean samples of Hα emitters in the four redshift slices (Sobral et al. 2013). The excess narrow-band flux is then converted into an emission line luminosity. For the analyses in this paper, we take these cleaned catalogues and introduce cuts to ensure that the data in each narrow-band filter are complete to the same flux limit across the entire area observed. These final catalogues contain: 428 Hα emitters at $z = 0.40$, 595 at $z = 0.84$, 420 at $z = 1.47$ and 372 at $z = 2.23$ down to the SFR limits $\sim$0.2, 3.0, 12.0 and 25.0 $M_\odot\,yr^{-1}$, respectively (assuming $A_{H\alpha} = 1.0$), to an Hα equivalent width lower limit of 25 Å.

The SFRs for the HiZELS sample are calculated from the Hα luminosity and the relation of (Kennicutt 1998) [$SFR(M_\odot\,yr^{-1}) = 7.9 \times 10^{-42} L(H\alpha)\,(erg\,s^{-1})$], assuming a dust extinction $A_{H\alpha} = 1$ mag (see Sobral et al. 2013). Stellar masses are computed by fitting SEDs to the rest-frame UV, optical and near-infrared data available (*FUV*, *NUV*, *U*, *B*, *g*, *V*, *R*, *i*, *I*, *z*, *Y*, *J*, *H*, *K*, 3.6, 4.5, 5.8 and 8.0 μm collated in Sobral et al. 2013, and references therein), following Sobral et al. (2011) and the reader is referred to that paper for more details. The SED templates are generated with the Bruzual & Charlot (2003) package using Charlot & Bruzual (2007, unpublished) models, a Chabrier (2003) initial mass function and an exponentially declining star formation history with the form $e^{-t/\tau}$, with τ in the range 0.1 Gyr to 10 Gyr. The SEDs were generated for a logarithmic grid of 200 ages (from 0.1 Myr to the maximum age at each redshift being studied). Dust extinction was applied to the templates using the Calzetti et al. (2000) law with $E(B - V)$ in the range 0 to 0.5 (in steps of 0.05), roughly corresponding to $A_{H\alpha} \sim 0$–2. The models are generated with different metallicities, including solar; the reader is referred to Sobral et al. (2011) for further details. For each source, the stellar mass is computed as the median of stellar masses of the 1σ best fits over the range of parameters.

In Fig. 1 (left), we plot the number density of galaxies, from the combined UDS and COSMOS fields, above a stellar mass of $10^{10}\,M_\odot$ and a given SFR, against redshift. From this, we can see that for a given SFR limit the number density increases rapidly with redshift. This is a manifestation of the fact that a typical star-forming galaxy has a greater sSFR at higher redshift, forming stars more rapidly for a given mass. In order to look for trends with redshift, we therefore define a quantity which we term as the epoch-normalized star formation rate (ENSFR), which is the SFR of a galaxy divided by $SFR^*(z)$. $SFR^*(z)$ is the SFR derived from the quantity $L^\star_{H\alpha}$ found by fitting a Schechter function to the Hα luminosity function at a given redshift, which we take from Sobral et al. (2013). We note that normalizing the SFR to $SFR^*(z)$ accounts, to first order, for the increase in sSFR with redshift. However, significant evolution in either the slope of the SFR–stellar mass relation or the dust obscuration would invalidate this.

The values of SFR^* essentially double for each HiZELS redshift interval considered with $SFR^* \sim 7.0$, 14.0, 29.0 and 57.0 $M_\odot\,yr^{-1}$ for $z = 0.4$, 0.84, 1.47 and 2.23, respectively. Interestingly, this same behaviour is seen in the evolution of the typical sSFR from Elbaz et al. (2011) with $sSFR \sim 0.2$, 0.4, 0.8 and 2.0 yr^{-1}, again at these redshifts. We suggest that this is because the Hα luminosity (and thus SFR) function evolves significantly more than the stellar mass function.

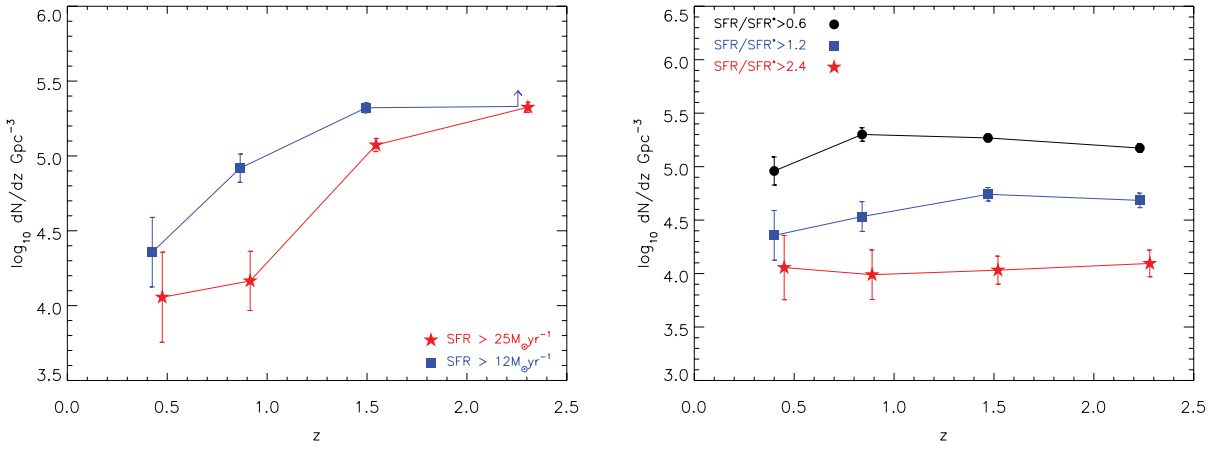

Figure 1. Left: the number density of HiZELS galaxies above a stellar mass of $10^{10}\,M_\odot$ and a given SFR plotted against redshift. The SFR $> 25\,M_\odot yr^{-1}$ lines are offset slightly in z for clarity. Right: the number density of $>10^{10}\,M_\odot$ galaxies above an ENSFR threshold. We define ENSFR as the ratio of SFR to $SFR^*(z)$ [with $SFR^*(z)$ derived from the $L^\star_{H\alpha}$, i.e. the typical SFR from the Hα luminosity function at that redshift; Sobral et al. 2013]. In this way, we remove the trend that the average sSFR of galaxies increases with redshift. As there is no evidence of a significant trend, this demonstrates that the number density of typical star-forming galaxies does not evolve significantly with redshift and thus the increase in the SFRD is purely an effect of increased typical sSFR.

In Fig. 1 (right), we plot the number density of galaxies of a given mass above the thresholds SFR/SFR$^\star(z) = 0.6,\ 1.2$ and 2.4. From this plot one can clearly see that the number of star-forming galaxies with their SFR normalized to the typical SFR at that epoch is broadly constant. This means that the number density of star-forming galaxies of a given mass and ENSFR does not evolve significantly over the period studied here. This demonstrates that the star-forming population is constant with redshift but simply evolves in sSFR. This is similar to the result found in (Sobral et al. 2013) in which there is no strong evolution in the Schechter parametrization of the normalization of the Hα luminosity function, $\phi^*_{\rm H\alpha}$. We discuss the implications of this in Section 5.

2.2 Imaging data

In this study we analyse near-infrared imaging from the space-based *HST*/WFC3 Cosmic Assembly Near-infrared Deep Extragalactic Legacy Survey (CANDELS; Grogin et al. 2011; Koekemoer et al. 2011) and the ground-based UKIDSS UDS and the WIRCam Deep Survey (WIRDS; Bielby et al. 2012).

The CANDELS imaging we use is from WFC3 F160W covering a two-orbit depth over 720 square arcmin of the UDS. The CANDELS imaging has a pixel scale of 0.06 arcsec and a point spread function (PSF) with a full width at half-maximum (FWHM) of 0.18 arcsec. The CANDELS data are well suited to this project for which we require high-resolution imaging in the rest-frame optical; however, to obtain the wider area coverage needed to build up a statistical sample of rarer high-mass systems from HiZELS we also need to use ground-based near-infrared imaging.

The UKIDSS UDS *K*-band imaging covers an area of 0.8 square degrees, to a depth of $K = 24.6$ (5σ, AB) with a pixel scale of 0.13 arcsec and a PSF FWHM of 0.7 arcsec. The WIRDS *K*-band imaging covers a total effective area of 2.1 square degrees and reaches an AB 50 per cent completeness limit of $\sim$24.5 across the COSMOS field, it has a pixel scale of 0.15 arcsec and a PSF FWHM of 0.7 arcsec and is thus comparable to the UKIDSS UDS.

The combination of these three near-infrared imaging data sets allows us to probe the rest-frame optical morphologies and sizes of the HiZELS galaxies over a wide range in luminosity while at the same time providing a rest-frame optical view of the galaxies' stellar distribution.

3 ANALYSIS

3.1 Sizes

Before studying the morphologies and the merger rates of the galaxies in the HiZELS sample, we first assess their typical sizes. This is interesting from a galaxy evolution perspective, as an increase in size with cosmic time may imply that mass is being built up either through mergers or accretion or that the mass is being redistributed somehow. If there is no direct evolutionary connection between the galaxy populations at each epoch then changes in typical size may suggest differing formation scenarios. Importantly, it will also help us to understand the reliability of the morphological classification as the smallest galaxies will be most affected by the resolution of our ground-based imaging.

The surface photometry of galaxies is often described by a Sérsic profile (Sérsic 1968).

$$I(r) = I_e \exp\left\{-b_n\left[\left(\frac{r}{r_e}\right)^{1/n} - 1\right]\right\}, \quad (1)$$

where $I(r)$ is the intensity, r is the radius from the centre of the galaxy, r_e is the scale radius, I_e is the intensity at r_e, n in the exponent is a free parameter widely known as the Sérsic index and $b_n = 2n - 0.327$; a coefficient chosen so that r_e is the half-light radius defined as the radius which encircles half the light from the galaxy (e.g. Graham et al. 1996).

To measure the sizes of the galaxies we fit a two-dimensional Sérsic profile to the galaxy images using the GALFIT (version 3) software package (Peng et al. 2002). This software requires reasonable initial input parameters such as position, apparent magnitude and ellipticity, all of which are estimated by first running the SExtractor package (Bertin & Arnouts 1996) so that the iterative fitting process converges to the correct solution in the shortest possible time. GALFIT deconvolves the PSF which is dominated either by the telescope itself, in the case of *HST*, or by the atmospheric seeing for the ground-based imaging. To this end, we check that the effect of seeing has been correctly accounted for in the analysis of the ground-based imaging by comparing the CANDELS derived sizes to those from the UKIDSS UDS imaging for the same galaxies. Fig. 2, shows this comparison of galaxy sizes for a sample drawn from a combination of all four HiZELS redshift slices and a sample of *BzK* (Daddi et al. 2004) galaxies in the UDS field (the photometry to select *BzK* galaxies is taken from the UDS catalogues; Almaini et al., in preparation). These two independent size measurements are correlated and scattered around the one-to-one line with $\Delta r_e/r_e \sim 0.4$, which confirms that the sizes recovered are comparable, demonstrating that GALFIT is able to successfully account for the seeing.

We note that there may be some selection effects and biases in size measurements, in that galaxies with large sizes can be missed due to low surface brightnesses and compact galaxies may have sizes overestimated (Barden et al. 2005). The former is less likely as the HiZELS galaxies are selected on their Hα emission. Also, Fig. 2 demonstrates that there is no significant bias in size estimates between the ground- and space-based analysis of the smallest galaxies so we take this as evidence that their sizes are not overestimated.

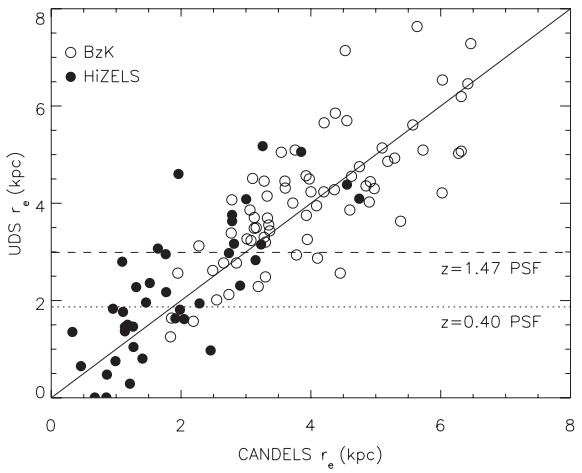

Figure 2. The half-light radius measured from the UKIDSS UDS ground-based imaging plotted against that from the *HST*/WFC3 CANDELS data at all redshifts. The solid line is the one-to-one line. The open and filled circles represent *BzK* and HiZELS galaxies, respectively. The dashed and dotted lines represent the UKIDSS UDS PSF half width half maximum (HWHM) at $z = 1.47$ and 0.4, respectively, which bracket the other two epochs. This demonstrates that we can recover the sizes of galaxies by accounting for the ground-based PSF using GALFIT (Peng et al. 2002).

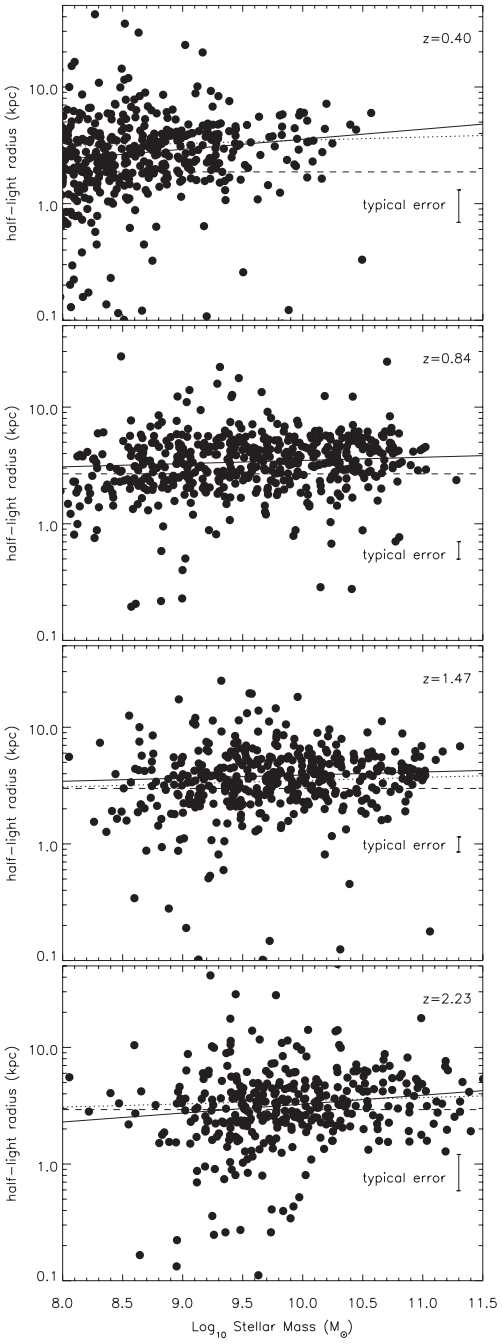

Figure 3. The half-light radius plotted against stellar mass for $z = 0.4$ (top), 0.84 (upper middle), 1.47 (lower middle) and 2.23 (lower). The solid lines are linear fits to the relations with the dotted line, the $z = 0.84$ fit for reference. The dashed lines represent the PSF HWHM. The slope of the size–mass relation is found to be broadly constant.

Fig. 3 shows the size–mass relations at each redshift slice. We perform linear fits to this relation of the form $\log_{10} r_e = a\,(\log_{10}(M_*) - 10) + b$, where r_e and M_* are in units of kpc and $M_\odot$, respectively, and we normalize the fits to $M_* = 10^{10}\,M_\odot$. Table 1 contains the results of these fits at the four redshift slices considered. From these fits we find the surprising result that the typical size of a star-forming galaxy with $\log_{10} M_* = 10$ does not evolve significantly out to $z = 2.23$, with $r_e = 3.6 \pm 0.3$ kpc on average. These results are in good agreement with the trends of Barden et al. (2005) and Ichikawa, Kajisawa & Akhlaghi (2012) who also find little evidence of an evolution in this relation or the typical size of star-forming galaxies. In a related study, Kanwar et al. (2008) find no evolution in the shape of the size function of disc galaxies in the range $0.1 < z < 1.0$ with just an evolution in the number density of discs. However, other groups have found evidence for a stronger size evolution for the most massive ($M_* > 10^{10}\,M_\odot$) disc-like galaxies, with a 2–4 fold increase in size since $z \sim 2$ (Trujillo et al. 2007; Mosleh et al. 2011).

Table 1. The size–mass relations at each redshift slice, of the form $\log_{10} r_e = a\,(\log_{10}(M_*) - 10) + b$. Where r_e and M_* are in units of kpc and $M_\odot$, respectively.

z	a	b	r_e at $\log_{10}(M_*) = 10$ (kpc)
0.40	0.08 ± 0.02	0.55 ± 0.03	3.6 ± 0.2
0.84	0.03 ± 0.02	0.54 ± 0.01	3.5 ± 0.1
1.47	0.03 ± 0.02	0.59 ± 0.01	3.9 ± 0.2
2.23	0.08 ± 0.03	0.51 ± 0.02	3.3 ± 0.2

By analysing the Sérsic index, n, which we obtain from the fitting process, we divide our sample into disc-like and bulge-like galaxies where we define the former as having $0.5 \leq n < 2.5$ and the latter as $2.5 \leq n < 5.0$. From this, we find that the fraction of disc-like galaxies is >80 per cent in each redshift slice with no evidence for an evolution, which is not unexpected as star-forming galaxies such as those selected by HiZELS are in general found to be discs, consistent with Sobral et al. (2009). We note that this disc fraction also has no trend with SFR or stellar mass.

3.2 Morphologies

3.2.1 Quantifying and calibrating morphology

To quantify the morphologies of the galaxies in this study we choose to use a combination of Gini and M_{20} coefficients first proposed by Lotz et al. (2004). The Gini coefficient, developed by statistician Corrado Gini, measures the inequality among values of a frequency distribution. It was first applied to studies of galaxy morphology by Abraham, van den Bergh & Nair (2003). A Gini coefficient of zero expresses an equality where all values are the same (i.e. a galaxy with uniform surface brightness). A Gini coefficient of 1 expresses maximal inequality among values (i.e. where all of the flux is in 1 pixel element^{-1}). The M_{20} coefficient, describes the second-order moment of the brightest 20 per cent of pixels in the galaxy and is sensitive to merger signatures such as multiple nuclei (Lotz et al. 2004). The combination of Gini and M_{20} can differentiate between 'normal' star-forming galaxies and ultraluminous infrared galaxies, as well as single galaxies and merging systems. However, there are some differences in the boundaries chosen to delineate these populations (e.g. see Lotz et al. 2006, 2008) and therefore we choose to perform our own tests and calibrate the Gini and M_{20} coefficients by visual inspection.

The Gini and M_{20} coefficients are calculated using the Gini and M_{20} components of the GALVSM software (Huertas-Company et al. 2008). This software requires a segmentation map which tells GALVSM which pixels are associated with the galaxy. We first cutout 10 arcsec postage stamp images, taken from the CANDELS mosaic, around each galaxy and generate a segmentation map using SExtractor (Bertin & Arnouts 1996). The Gini and M_{20} codes are

then run on the postage stamps and the corresponding segmentation maps.

The sample we choose to run the initial visual inspection calibration analysis on is that of 167 star-forming galaxies in the redshift range $1.4 < z < 2.5$ selected via the *BzK* method (Daddi et al. 2004) which lie within the CANDELS survey region in the UDS. The F160W mosaic provides high-resolution rest-frame optical imaging of these galaxies. We choose this sample over the HiZELS narrow-band sample as it should consist of similar star-forming galaxies but has a higher surface density and so a larger sample falls within the high-resolution CANDELS imaging, key to testing the morphological classifications.

From visual inspection of the *BzK* galaxy morphologies, the SExtractor parameters DEBLEND_MINCONT=0.1 and DETECT_MINAREA=5 and DETECT_THRESH=1 σ are found to be relaxed enough to associate clear merging components of the same 'galaxy' with one segmentation map but still stringent enough so as to not produce clear false positives. We note that having a DEBLEND_MINCONT set too high means that unrelated galaxies would be considered as mergers whereas when set to a low value separate features within the same galaxy separate into distinct objects and therefore this parameter has the most effect on the M_{20} coefficient (see Appendix A for a discussion of this parameter). Setting the detection threshold to low sigma values includes fainter 'sky' pixels in the segmentation map and thus increases inequality, raising the Gini coefficient. In this way, one can see that the way in which the segmentation map is created is the most important factor in determining the Gini and M_{20} coefficients and differences between how this is done in different studies are the reason why we choose to calibrate our own definitions of mergers and non-mergers.

Using the above method, fixing the SExtractor parameters to those found to give the best performance, the Gini and M_{20} codes are run on the CANDELS imaging with the results for the *BzK* sample displayed in Fig. 4 (upper). Also included is a $0.35 < z < 0.45$ photometric redshift sample with a similar magnitude range to the HiZELS $z = 0.40$ sample sourced from Williams et al. (2009) to demonstrate that this classification technique is not affected by redshift.

By visually assigning the galaxies into two categories 'mergers' and 'non-mergers' with the former classification based on evidence of merging components either creating disturbed morphologies or very close potential mergers (on-sky separation $\lesssim 2$ arcsec). This information is included in Fig. 4, with the delineation between mergers and non-mergers found to occur at $M_{20} \sim -1.5$ for both high- and low-redshift regimes and thus the Gini coefficient does not seem to add any information. Using this method there is a contamination of $\sim$10 per cent non-mergers in the mergers and $<$5 per cent mergers in the non-mergers. The simulations performed for Appendix A demonstrate that the M_{20} coefficient is sensitive to merging components down to a luminosity (mass) ratio of $\sim$1: 10 (in agreement with the simulations of Lotz et al. 2010). As such we note that our analysis throughout this paper is a measure of major mergers only.

The morphology codes are then run on the same galaxies but using the deep *K*-band ground-based UKIDSS UDS so we can compare the two independent measurements. We expect the higher resolution CANDELS imaging to be a truer reflection of a galaxy's intrinsic morphology. We also note here that it is difficult to measure the morphologies of the lowest luminosity galaxies in our sample as they tend to be smaller (see size–mass relations in Section 3.1) and are thus more affected by the seeing of the ground-based near-infrared imaging. By performing tests we find that setting

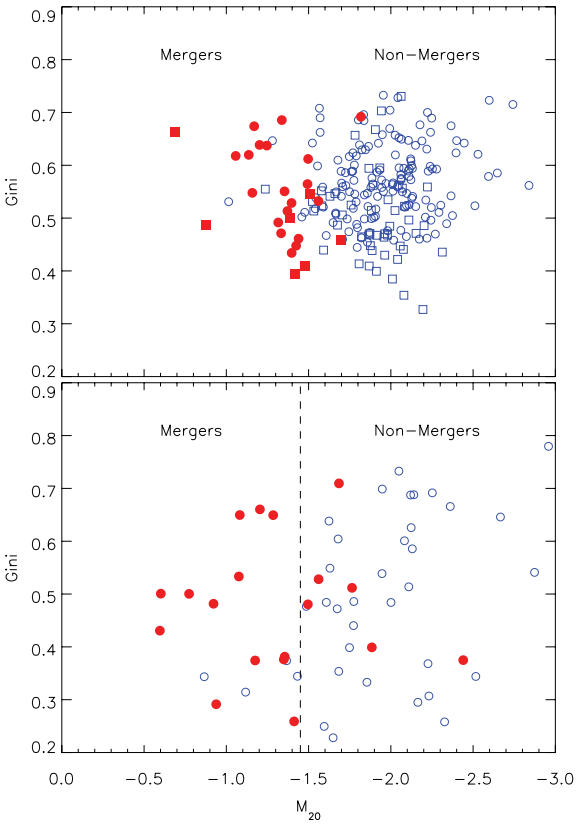

Figure 4. Upper: the Gini coefficient plotted against the M_{20} value for the $z \sim 1.4$–2.5 *BzK* population and a photometric redshift sample with $z \sim 0.4$ from the F160W CANDELS imaging data in the UDS field. The filled red and open blue symbols are those classified as mergers and non-mergers, respectively, by visual inspection of the CANDELS imaging with circles representing mergers and non-mergers for the *BzK* population and squares for the $z \sim 0.4$. From visual inspection $M_{20} \sim -1.5$ appears to be an excellent delineation between mergers and non-mergers. This demonstrates that for our particular analysis the key parameter for determining whether a galaxy has a merger-like morphology is the M_{20} parameter and not the Gini coefficient. Lower: the Gini coefficient plotted against the M_{20} coefficient for HiZELS galaxies at all redshifts, as measured from the UDS *K*-band imaging and calibrated using equations (2) and (3) but with morphologies visually identified from the CANDELS F160W image. The filled red and open blue circles are those visually classified as mergers and non-mergers, respectively. The vertical line at $M_{20} = -1.45$ is the value we now choose from visual inspection to delineate the mergers and non-mergers. This demonstrates that the calibrated ground-based near-infrared imaging can be used to derive M_{20} values that differentiate between mergers and non-mergers.

DEBLEND_MINCONT=0.03 ensures that the M_{20} parameter selects the same type of mergers in the ground-based data as that derived from the *HST* data (again see Appendix A). The ground-based versus *HST* Gini and M_{20} values are plotted in Fig. 5. By performing linear fits to these relations we can calibrate the ground-based Gini and M_{20} values to those derived from *HST*. These fits are

$$\mathrm{Gini}_{\mathrm{CANDELS}} = 0.78\,\mathrm{Gini}_{\mathrm{UDS}} + 0.13 \quad (2)$$

$$M_{20,\mathrm{CANDELS}} = 0.68\,M_{20,\mathrm{UDS}} - 0.39 \quad (3)$$

and will now be applied to the HiZELS morphologies derived from the ground-based near-infrared imaging.

One potential problem with measuring the morphologies of galaxies at different epochs, using the same near-infrared

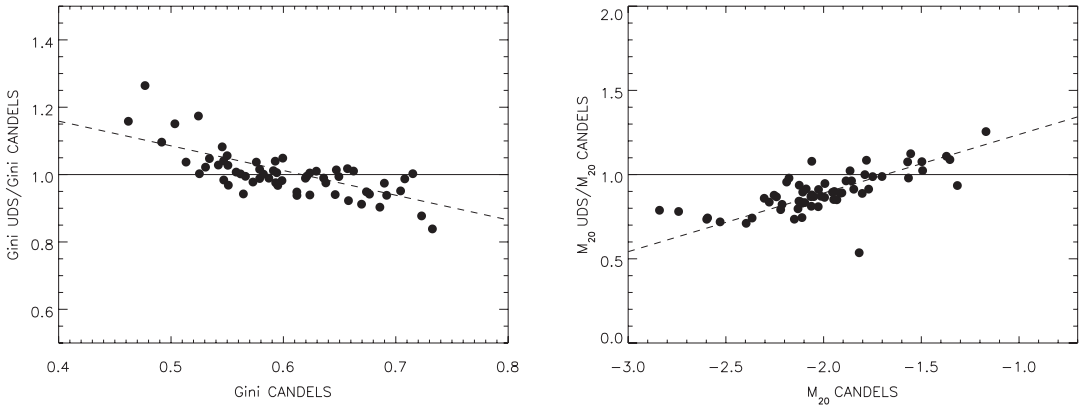

Figure 5. Left: the ratio of the Gini coefficient for *BzK* galaxies measured from the UKIDSS UDS ground-based *K*-band imaging to that measured from the CANDELS *HST* F160W imaging plotted against the Gini coefficient measured from the CANDELS F160W imaging. The solid line is the one-to-one relation and the dashed line is a fit to the observed trend. Right: the ratio of the M_{20} coefficient for *BzK* galaxies measured from the UKIDSS UDS ground-based *K*-band imaging to that measured from the CANDELS F160W imaging plotted against the M_{20} coefficient measured from the CANDELS F160W imaging. The solid line is the one-to-one locus and the dashed line is a fit to the relation. From these plots we can see that it is possible to calibrate the values of Gini and M_{20} derived from ground-based imaging to those from *HST* imaging.

imaging, is that of morphological *k* correction. Galaxies look smoother at longer wavelengths, meaning that the lowest redshift galaxies in our sample may artificially appear less disturbed than those at high redshift. When we analyse the *HST* Advanced Camera for Surveys (ACS) F814W imaging data available in COSMOS, many of the galaxies are very low surface brightness and therefore it is difficult to assess whether the morphological classifications given by the M_{20} coefficient are reliable. However, for the galaxies in the $z = 0.4$ sample with $K_{\rm AB} < 22.5$, the same classifications as those derived from the near-infrared CANDELS imaging are recovered in ∼90 per cent of the cases, so we conclude that our results are not significantly affected by this.

An additional concern is that some disc galaxies at high redshift are found to contain large star-forming clumps (e.g. Swinbank et al. 2010b, 2012). There may therefore be a degeneracy between what we classify as 'mergers' and those galaxies that contain a small number of large star-forming clumps. It is practically impossible to differentiate between these two populations without dynamical information and thus we note with caution that so-called clumpy disc galaxies may make up some fraction of our 'merger' sample, if the clumps are on scales of $\gtrsim$4 kpc. In fact, when we run the subsample of nine HiZELS galaxies which, from dynamical analysis of integrated field unit data, are all found to contain clumps (see Swinbank et al. 2012 for a description of this sample) all of them have $M_{20} \gtrsim -1.5$ and thus we would classify them as 'mergers'. We note here that when visually classified, not all of these clumpy galaxies appear as clear mergers which may explain the non-merger interlopers with $M_{20} \gtrsim -1.5$ in Fig. 4.

3.2.2 HiZELS morphologies

The number densities of galaxies in the HiZELS samples are lower than the *BzK* morphology calibration sample used in Section 3.2.1 and therefore do not have the same level of overlap with the CANDELS imaging region in the UDS. We instead run the morphology codes on the CANDELS, UKIDSS UDS and COSMOS WIRDS imaging for the HiZELS samples at each of the four redshifts. The output Gini and M_{20} values for the ground-based near-infrared imaging are calibrated to the CANDELS values using the fits found for the *BzK* sample in Section 3.2.1. As a confirmation of the calibration of the ground-based morphologies to those derived from the *HST* data the UKIDSS UDS Gini and M_{20} coefficients for those that line in the CANDELS subregion are plotted in Fig. 4 (lower) but with the visual classifications derived from the CANDELS data indicated. The result of analysing the morphologies of these calibrated data is that we now choose to delineate the difference between mergers and non-mergers at $M_{20} = -1.45$ which minimizes the visual contamination to 22 ± 12 per cent non-mergers in the merger region and 15 ± 7 per cent mergers in the non-merger region. We note that some of the contamination of visually classified non-mergers to the merger fraction may in fact be due to galaxies with clumpy discs (see Section 3.2.1). Fig. 6, displays a subsample of the HiZELS galaxies classified by the M_{20} parameter as mergers (left) and non-mergers (right) for both ground- and space-based imaging, with their SExtractor segmentation maps overplotted. As the Gini coefficient is found to add little information, when using our particular analysis methods, Fig. 7 presents a histogram of M_{20} values, as measured from the ground-based imaging of the HiZELS population at all redshift slices.

4 RESULTS

4.1 Merger fractions

Here, we define 'merger fraction' as the number of galaxies with a merger-like morphology (regardless of how many galaxies actually make up this merger) divided by the total number of galaxies in the redshift slice. The total fraction of mergers for the HiZELS galaxies in the redshift bins $z = 0.40, 0.84, 1.47, 2.23$ are 0.33, 0.13, 0.18 and 0.32, respectively (see Fig. 7); however, these are not comparable as they are measured for different stellar mass and SFR ranges at the different redshifts.

For comparison Sobral et al. (2009) find a higher merger fraction of 0.28 at $z = 0.84$ using the morphological classifications of Scarlata et al. (2007) and a visual classification that included mergers and close pairs (which explains the higher merger fraction), although this is from rest-frame *B*-band imaging. However, when we study the COSMOS *HST* ACS imaging used in that study we find that many of the galaxies appear as very low surface brightness meaning that their morphological classifications are more uncertain.

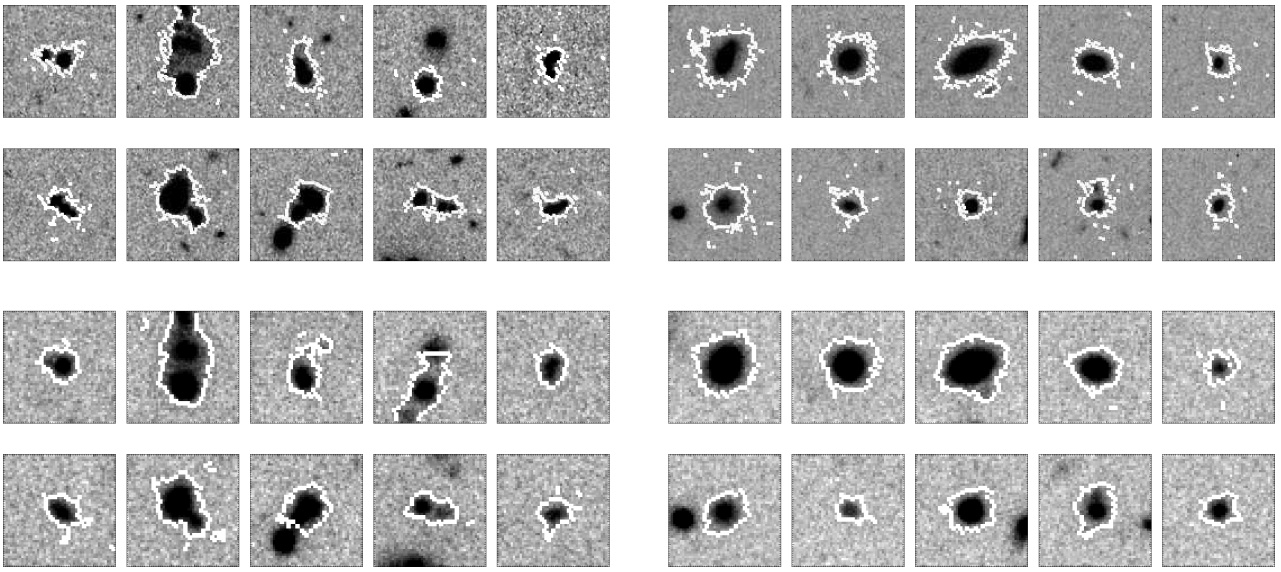

Figure 6. Left: postage stamp images (10 arcsec × 10 arcsec) from both CANDELS *HST* F160W (upper 10) and UDS *K* (lower 10) of the same HiZELS galaxies classified by M_{20} as major mergers. Right: postage stamp images (10 arcsec × 10 arcsec) from both CANDELS F160W (upper 10) and UDS *K* (lower 10) of the same HiZELS galaxies classified by M_{20} value as non-mergers. It is clear from this plot that mergers are well separated from non-mergers in this morphological classification system and that it is possible to identify mergers from the ground-based imaging. The white outlines represent the SExtractor segmentation maps used for the morphological analysis.

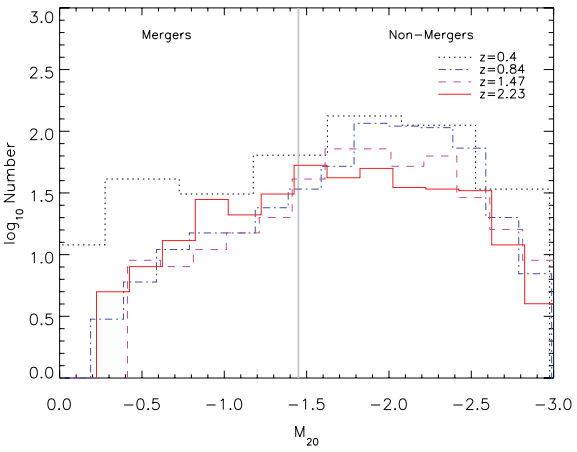

Figure 7. A histogram of M_{20} values for the four HiZELS redshift slices. The vertical line at $M_{20} = -1.45$ delineates mergers from non-mergers.

In Fig. 8 (left), the merger fraction is plotted against stellar mass, with the lowest mass galaxies progressively more likely to be classed as mergers with ∼5–20 per cent of the star-forming population being mergers at the highest stellar masses in each of our redshift slices. The $z = 0.4$, 0.84 and 1.47 trends are all remarkably similar and in agreement but there is an increase in merger fraction at all masses to $z = 2.23$. However, the HiZELS selection is dependent on SFR, not mass and as described in Section 2 the typical sSFR for galaxies increases with redshift and therefore we need to investigate these effects too.

A fraction of 10–20 per cent mergers is seen in the most strongly star-forming galaxies at each redshift (Fig. 8, centre). However, due to the flux-limited nature of the samples and the evolution of typical sSFR there is little overlap between different redshifts. In this figure, the combined SFR data for all of the HiZELS redshift bins taken at face value may actually hint at a trend in merger fraction with SFR rather than any evolution with redshift (at least out to $z = 1.47$). There is some evidence of an increase in merger rate at the same SFR when going from $z = 1.47$ to $z = 2.23$ but again this does not account for the evolution in typical sSFR.

Combining the two results above we investigate the relative contribution of mergers to the range of sSFR covered by our sample, for galaxies with ENSFR > 0.2 to which we are complete at all redshifts, in Fig. 8 (right). From this plot it is clear that the galaxies with the higher sSFR at all redshifts are increasingly more likely to have a merger-like morphology, with those with the highest sSFR having a merger fraction of ∼40–50 per cent. This strongly suggests that starbursts are more likely to be driven by major mergers when compared to the rest of the star-forming population. This is in agreement with the far-infrared selected sample of Kartaltepe et al. (2012) who find that major mergers have, on average, a high sSFR compared to typical star-forming galaxies. It is also in broad agreement with results from the mass selected sample of (Kaviraj et al. 2012) who also find that major mergers tend to have high sSFR compared to undisturbed galaxies.

We test whether the $A_{H\alpha} = 1.0$ dust correction we universally employ is reasonable and how it affects our results. This is by including both SED fit extinction values (Sobral et al. 2013) and those derived from the relation between stellar mass and extinction from Garn & Best (2010). We find that using these more sophisticated estimates makes little difference for the range of masses we study. The value of $A_{H\alpha}$ is ∼1 mag at a mass of $10^{10}M_{\odot}$ with this value increasing/decreasing to higher/lower mass, with the typical range being $A_{H\alpha} = 0.5$–2 mag. In fact, when this more sophisticated treatment of dust obscuration is included it acts to strengthen our conclusions by smoothing the relations in Fig. 8. However, we choose to keep the extinction value at $A_{H\alpha} = 1.0$ as this is easier to compare to other works including the main results in Sobral et al. (2013) and to 'epoch normalize' with the Hα luminosity function.

It is unlikely that HiZELS is missing a large population of 'typical' high-redshift star-forming galaxies with high dust obscurations, as Reddy et al. (2012) demonstrate that the dust content of typical star-forming galaxies actually decreases with redshift. However,

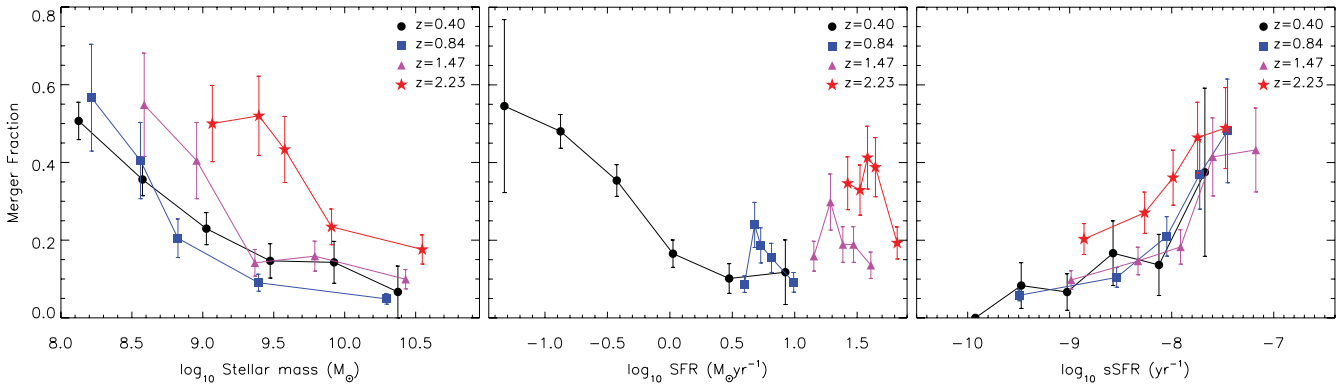

Figure 8. Left: fraction of M_{20} identified mergers versus stellar mass for the four HiZELS redshift slices. Centre: fraction of M_{20} identified mergers versus SFR for the four HiZELS redshift slices. From these plots we can see that the merger fraction depends on mass and perhaps SFR with the most massive and most star-forming galaxies having the lowest merger fractions. Right: fraction of M_{20} identified mergers versus sSFR for galaxies with ENSFR > 0.2 for the four HiZELS redshift slices. This suggests that major mergers can lead to galaxies having unusually high sSFR compared to the typical value at a given mass and redshift.

the HiZELS sample may miss extreme star-forming and highly obscured galaxies such as submillimetre galaxies. Submillimetre galaxies are found to have a spread in morphologies which is indistinguishable from that of typical star-forming galaxies at high redshift (Swinbank et al. 2010a) and are relatively rare objects ($1–2 \times 10^{-5}$ Mpc^{-3}; Wardlow et al. 2011), thus their omission would not affect our conclusions.

4.2 Merger rates

To calculate the merger rates (the number of mergers per Gpc^3 per Gyr) we follow the prescription outlined in Lotz et al. (2011): that the merger rate is simply the number of mergers per Gpc^3 divided by the average time-scale over which the merger would be observed. In Lotz et al. (2011) this observed merger time-scale is found, from simulations, to be ∼0.2 Gyr, when the Gini/M_{20} method is employed. We adopt this value for consistency with that study and with the data from other groups recalculated and used there. We note that as HiZELS is a narrow-band survey the volumes covered at each redshift slice are well defined with values of $\sim 1-7 \times 10^{-4}$ Gpc^3 (Sobral et al. 2013). We now also assume that there are on average two galaxies per merger for consistency with other studies.

For comparison with other surveys we initially cut our sample only on stellar mass. The merger rates for galaxies with $M > 10^9$ and 10^{10} M$_\odot$ are plotted in Fig. 9 (left). Also plotted are values from Conselice et al. (2003) ($M_B < -19$ which approximates $M > 10^9$ M$_\odot$) and those with $M > 10^{10}$ M$_\odot$ derived from Gini/M_{20} (Lotz et al. 2008), close pairs (Lin et al. 2008) and galaxy asymmetry from Conselice et al. (2009) and López-Sanjuan et al. (2009). These merger rates are corrected to the time-scales calculated by Lotz et al. (2011) using the galaxy evolution models of Somerville et al. (2008).

Fig. 9 (left) shows little evolution in merger rate with redshift and the results are generally in good agreement with those found in the studies of Conselice et al. (2003), Conselice et al. (2009), Lin et al. (2008) and López-Sanjuan et al. (2009), where the redshift ranges overlap. The merger rates from Lotz et al. (2008) are systematically higher, which may be because sample is mass selected and therefore includes a significant contribution from merging red sequence galaxies which would not have been included in the HiZELS sample. There could also be secondary effects due to a mismatch in the stellar mass calculation between the studies, a different way of defining mergers through the M_{20} parameter or a differential in the time-scales involved, so an offset is perhaps not unexpected. With the exception of the $z = 0.4$ data point, which is significantly higher, the HiZELS merger rates for galaxies with $M > 10^9$ M$_\odot$ are also in good agreement with those of the only study with this approximate mass limit (Conselice et al. 2003). From this plot there is no strong evidence for an increase in the merger rate for mass-selected samples out to $z \sim 2$. However, this comparison does not account for the SFR limits of the different surveys or the increase in typical sSFR with z (Elbaz et al. 2011).

The advantage of HiZELS over these earlier studies is that it is unbiased with respect to stellar mass and we derive the stellar mass and SFR from independent measurements, i.e. SED fitting and Hα flux. We can therefore consider both SFR and stellar mass independently to split the population into subsamples based on these properties. As defined in Section 2 we account for the increase in the typical sSFR with redshift by employing the ENSFR. Fig. 9 (right) shows the population split into three ENSFR bins >0.6, 1.2 and 2.4, for which the HiZELS observations are complete at all redshifts. The first obvious thing to note is that undulating shape of the plot with just a mass cut (Fig. 9, left) has disappeared. Instead the trends are flat, showing no evidence for an increase in the merger rate with increasing redshift for all masses and ENSFR cuts. This mass and ENSFR selected sample is a cleaner sample than those in Fig. 9 (left) and so we suggest that the peak in the merger rate at $z \sim 1$ seen for some comparison samples may be due to the mixing of a mass limit with an SFR selection function which strongly effects photometrically selected galaxies.

From this merger analysis, we can determine the total number of major mergers (with mass ratio >1: 10) a galaxy of a given mass will undergo during the epoch covered by our study. Using equation 11 from (Conselice 2006) we find that one would expect ∼3 mergers per star-forming galaxy with $M \sim 10^{10}$ M$_\odot$ between $z = 2.23$ and 0.4, or a merger every 2 Gyr on average. We note that these numbers depend on the value of τ the time-scale over which mergers can be observed using the M_{20} method (which we assume to be 0.2 Gyr; Lotz et al. 2011) and therefore more generally there are $0.6\tau_0\tau^{-1}$ mergers between $z = 2.23$ and 0.4, corresponding to $0.1\tau_0\tau^{-1}$ mergers per Gyr, where $\tau_0 = 1$ Gyr.

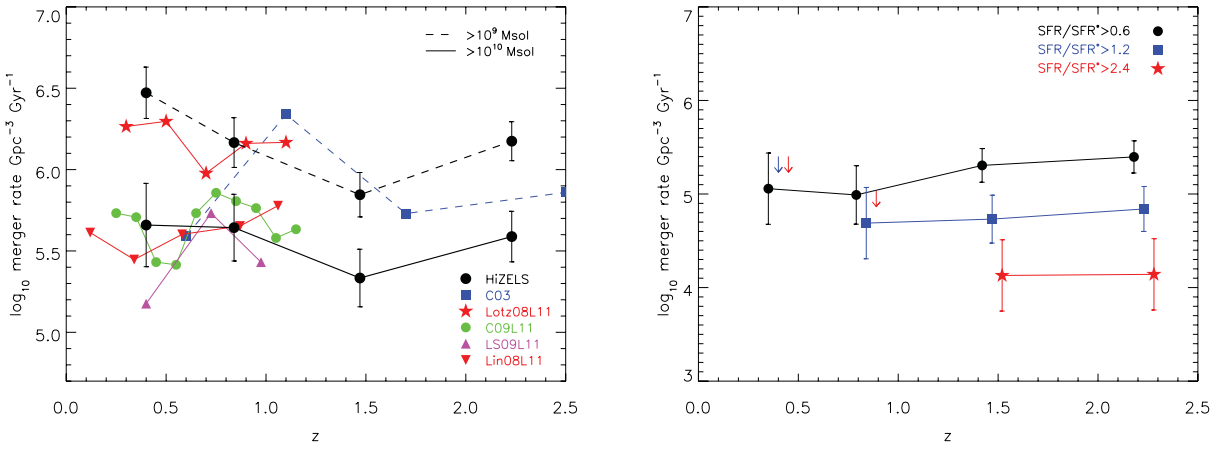

Figure 9. Left: merger rates for the HiZELS sample above a given mass against redshift. For comparison, we include merger rates derived from: close pairs (Lin et al. 2008, Lin08L11); Gini/M_{20} (Lotz et al. 2008, Lotz08L11); and galaxy asymmetry (Conselice et al. 2003, 2009; López-Sanjuan et al. 2009, labelled C03, C09L11 and LS09L11, respectively). The L11 denotes that these merger rates were originally sourced from their respective papers but have been corrected to the time-scales calculated by Lotz et al. (2011) using the galaxy evolution models of Somerville et al. (2008). The samples of Lin08L11, Lotz08L11, C09L11 and LS09L11 are all at $M_* > 10^{10}$ M$_\odot$ while C03 is $M > 10^9$ M$_\odot$. Right: the merger rates for HiZELS galaxies with $M_* > 10^{10}$ M$_\odot$ above a given ENSFR (ENSFR = SFR/SFR*(z)). The points are offset by Δz for clarity. From these plots one can see that there is no evidence for a significant evolution in merger rate when both the mass and the ENSFR of the galaxies are accounted for in the selection.

5 DISCUSSION AND CONCLUSIONS

The HiZELS narrow-band Hα survey selects star-forming galaxies within four well-defined volumes at $z \sim 0.4$–2.2 and flux limits with an SFR indicator which is unbiased in terms of stellar mass and is independent of its determination. In this paper, we have used these properties to understand the star-forming population and its merger rate to help illuminate the processes responsible for the up-turn in the SFRD with redshift.

By defining the ENSFR (ENSFR = SFR/SFR*(z)) we account for the increase in the typical SFR of galaxies with redshift. In Section 2, we demonstrate that the number of galaxies above a given mass and ENSFR does not evolve significantly over 6 Gyr from $z = 0.4$ to 2.23. We also note that the HiZELS sample has already been shown to accurately trace the increase of the SFRD with redshift and that there is no strong evolution in the normalization of the Hα luminosity function (Sobral et al. 2013). Taken, in combination this means the increase in the SFRD with redshift is not due to an increase in the number of star-forming galaxies of a given mass but instead must result from an increase in the amount of star formation in these galaxies. This can be described as an increase in the average sSFR for star-forming galaxies (Rodighiero et al. 2010; Elbaz et al. 2011) without a significant increase in their number density. Also, we note that the SFR* (derived from $L^\star_{\rm H\alpha}$) evolves in the same way as the typical sSFR for star-forming galaxies (Elbaz et al. 2011), which implies that the luminosity of the knee in the Hα luminosity function is evolving significantly more rapidly than the characteristic mass of the stellar mass function.

The size–mass relation for galaxies is assessed in Section 3.1. In order to do this for a large sample we need to use wide-field ground-based imaging. Hence, we confirm that we can reliably recover the galaxy size determined from the *HST* CANDELS imaging by deconvolving the effect of atmospheric seeing from the ground-based imaging. We find that the size–mass relation is surprisingly constant out to $z = 2.23$, in agreement with the findings of Barden et al. (2005), Ichikawa et al. (2012) and at odds with the results of Trujillo et al. (2007) and Mosleh et al. (2011). The lack of strong size evolution at a given mass and the universal size–mass relation for star-forming galaxies in the range $0.4 < z < 2.23$ suggests that this population have not experienced significant size evolution, through mergers or star formation, during this period. Any evolution that does occur must thus act to move the galaxy along the locus of the relation. The slope of this relation is also shallow and thus low-mass galaxies are not dramatically smaller than their higher mass counterparts. Even if there is no direct evolutionary connection between the galaxy populations at each epoch then this lack of change in typical size suggests a universal evolution scenario.

In order to study the merger rates of the HiZELS galaxies we test the Gini and M_{20} coefficients. By investigating these automated methods of determining merger classifications we find that SExtractor parameters that define the segmentation map employed in these analyses are the most important factor in how well the method performs (see Appendix A). We find that, for the segmentation maps generated by our set of SExtractor parameters, the best delineation between mergers and non-mergers is $M_{20} = -1.45$ while the Gini coefficient provides no useful information. We acknowledge that other authors have found this not to be the case with M_{20} and Gini being equally important in morphological classification (Lotz et al. 2004; Wang et al. 2012) but we assume that this is due to the differences in the construction of the segmentation maps (see Appendix A) and potentially minor variations in the normalization of the M_{20} and Gini values, depending upon the exact nature of the morphological code used. The M_{20} coefficient is found to be sensitive to mergers down to a mass ratio of ∼1: 10 (in agreement with Lotz et al. 2010). We note here that not all mergers are star forming and as such we will miss 'dry' mergers which do not induce activity, although obviously these will not be major contributors to the SFRD. As with the sizes we find that it is possible to use this morphological classification on ground-based data affected by atmospheric seeing, after applying a calibration derived from galaxies that are observed with both ground-based telescopes and *HST*.

For the sample as a whole, without accounting for the Hα flux (SFR) limit or the increase in the sSFR of the star-forming galaxies with redshift, we find that the merger fraction anti-correlates with both stellar mass and SFR. By combining these two results we find that the merger fraction correlates strongly with sSFR. This suggests

that the more rapid the star formation is, the more likely it is to be driven by violent major mergers than secular processes. In fact we find that, ∼50 per cent, of starburst galaxies in our $z \sim 2$ sample have major merger morphologies. Therefore to achieve such high sSFR, these galaxies are undergoing major merger driven and not 'main sequence' star formation. Interestingly, we see no evolution in the merger fraction of starbursts with a constant ∼40–50 per cent across all redshifts which suggests that merging is a universal process that can lead to a galaxy having enhanced sSFR for their epoch (Hopkins et al. 2006; Kartaltepe et al. 2012).

Finally, we consider the merger rates of star-forming galaxies initially only limiting our sample on stellar mass, where some previous studies have seen the characteristic merger rate increase to $z \sim 1$. However, these other studies use photometrically selected samples where the method of determining stellar mass is directly linked to the determination of the SFR. As these two parameters are independent in HiZELS we can also select on SFR for a fair comparison across the redshift range, while also accounting for the increase in sSFR for typical star-forming galaxies with redshift. By applying these selections we see little evidence for an increase in the merger rates of typical galaxies over the redshift range considered. Therefore, even though there is an order of magnitude increase in typical SFR across the redshift range of our study this is not reflected in the merger rate. This is strong evidence that it is not major mergers that drive the increase in the SFRD with redshift, in contrast to the models of Somerville et al. (2001) or Hopkins et al. (2006) and as observed in part by Conselice et al. (2003, 2008) and Lin et al. (2008) who find some evidence for an increase in merging. Our result agrees with Sobral et al. (2009) who find that the increase in SFRD between $z = 0$ and 0.84 was primarily due to regular (non-merging) galaxies.

Depending on the time-scale τ for which it is possible to view a galaxy undergoing a major merger using the M_{20} parameter we find that star-forming galaxies with mass $>10^{10}\,\mathrm{M}_{\odot}$ undergo $\sim 0.6\tau_0\tau^{-1}$ (3 if $\tau = 0.2$ Gyr) mergers between $z = 2.23$ and 0.4, corresponding to $\sim 0.1\tau_0\tau^{-1}$ (0.5 if $\tau = 0.2$ Gyr) mergers per galaxy per Gyr, where $\tau_0 = 1$ Gyr. From analysis of the mass function of galaxies in COSMOS at $z = 0.35$–0.75, Pozzetti et al. (2010) find merger rates of ∼0.1–0.4 per galaxy per Gyr for galaxies with masses $\sim 10^{10.5}$–$10^{11}\,\mathrm{M}_{\odot}$, in reasonable agreement with our findings (both are very sensitive to the choice of τ). From a theoretical point of view Hopkins et al. (2010) compile data from a number of simulations and models (see references therein). The predicted number of mergers per galaxy with mass $\sim 10^{10}$–$10^{11}\,\mathrm{M}_{\odot}$ per Gyr is found to increase with redshift from a value of ∼0.05 at $z = 0.4$ to ∼0.25 at $z = 2.2$ apparently lower than the values we find. Again, this is dependent on τ so we are unable to provide solid constraints.

In summary, we find that the increase in SFRD is due to an increase in the sSFR of typical star-forming galaxies. The process responsible for this increase is not major mergers as we find that the merger rate does not increase in step with the SFRD. We therefore conclude that secular processes such as disc instabilities and/or an increase in the effective fuel for star formation are the main driver of the increase in the SFRD with redshift as predicted or observed by others (Kereš et al. 2005; Bower et al. 2006; Dekel et al. 2009; Förster Schreiber et al. 2011; Cacciato et al. 2012). Although we note that it could also be driven by an increase in the minor merger rate (mass ratios $<1:10$) which this study is not sensitive to.

We also find a constant merger fraction for starburst galaxies, in that around half are major mergers across all redshifts, demonstrating that extremely violent events are required for a galaxy to attain enhanced sSFR for their epoch and leave the 'main sequence'. Bringing these results together along with the lack of size evolution since at least $z = 2.23$ we can say that many of the properties of star-forming galaxies are surprisingly constant over the ∼6 Gyr covered in this study.

ACKNOWLEDGMENTS

We first thank the anonymous referee for improving the clarity of this paper. JPS acknowledges STFC for financial support. DS acknowledges the award of a NOVA fellowship. IRS acknowledges support from STFC and the Leverhulme Trust. We also thank James Mullaney and Mark Swinbank for useful discussions.

The United Kingdom Infrared Telescope is operated by the Joint Astronomy Centre on behalf of the Science and Technology Facilities Council of the UK.

Based on observations obtained with WIRCam, a joint project of Canada–France–Hawaii Telescope (CFHT), Taiwan, Korea, Canada, France, at the CFHT which is operated by the National Research Council (NRC) of Canada, the Institute National des Sciences de l'Univers of the Centre National de la Recherche Scientifique of France and the University of Hawaii. This work is based in part on data products produced at TERAPIX, the WIRDS consortium, and the Canadian Astronomy Data Centre. This research was supported by a grant from the Agence Nationale de la Recherche ANR-07-BLAN-0228.

This work is based on observations taken by the CANDELS Multicycle Treasury Programme with the NASA/ESA *HST*, which is operated by the Association of Universities for Research in Astronomy, Inc., under NASA contract NAS5-26555.

REFERENCES

Abraham R. G., van den Bergh S., Nair P., 2003, ApJ, 588, 218
Barden M. et al., 2005, ApJ, 635, 959
Bertin E., Arnouts S., 1996, A&AS, 117, 393
Best P. et al., 2010, preprint (arXiv:1003.5183)
Bielby R. et al., 2012, A&A, 545, A23
Bluck A. F. L., Conselice C. J., Bouwens R. J., Daddi E., Dickinson M., Papovich C., Yan H., 2009, MNRAS, 394, L51
Bower R. G., Benson A. J., Malbon R., Helly J. C., Frenk C. S., Baugh C. M., Cole S., Lacey C. G., 2006, MNRAS, 370, 645
Brinchmann J., Charlot S., White S. D. M., Tremonti C., Kauffmann G., Heckman T., Brinkmann J., 2004, MNRAS, 351, 1151
Bruzual G., Charlot S., 2003, MNRAS, 344, 1000
Cacciato M., Dekel A., Genel S., 2012, MNRAS, 421, 818
Calzetti D., Armus L., Bohlin R. C., Kinney A. L., Koornneef J., Storchi-Bergmann T., 2000, ApJ, 533, 682
Casali M. et al., 2007, A&A, 467, 777
Chabrier G., 2003, PASP, 115, 763
Cole S., Lacey C. G., Baugh C. M., Frenk C. S., 2000, MNRAS, 319, 168
Conselice C. J., 2006, ApJ, 638, 686
Conselice C. J., Bershady M. A., Dickinson M., Papovich C., 2003, AJ, 126, 1183
Conselice C. J., Rajgor S., Myers R., 2008, MNRAS, 386, 909
Conselice C. J., Yang C., Bluck A. F. L., 2009, MNRAS, 394, 1956
Cowie L. L., Songaila A., Hu E. M., Cohen J. G., 1996, AJ, 112, 839
Croton D. J. et al., 2006, MNRAS, 365, 11
Daddi E., Cimatti A., Renzini A., Fontana A., Mignoli M., Pozzetti L., Tozzi P., Zamorani G., 2004, ApJ, 617, 746
Daddi E. et al., 2007, ApJ, 670, 156
De Lucia G., Blaizot J., 2007, MNRAS, 375, 2
Dekel A., Sari R., Ceverino D., 2009, ApJ, 703, 785
Dressler A., 1980, ApJ, 236, 351
Elbaz D. et al., 2007, A&A, 468, 33
Elbaz D. et al., 2011, A&A, 533, A119

Förster Schreiber N. M. et al., 2009, ApJ, 706, 1364
Förster Schreiber N. M. et al., 2011, ApJ, 739, 45
Garn T., Best P. N., 2010, MNRAS, 409, 421
Garn T. et al., 2010, MNRAS, 402, 2017
Geach J. E., Smail I., Best P. N., Kurk J., Casali M., Ivison R. J., Coppin K., 2008, MNRAS, 388, 1473
Geach J. E., Smail I., Moran S. M., MacArthur L. A., Lagos C. d. P., Edge A. C., 2011, ApJ, 730, L19
Geach J. E., Sobral D., Hickox R. C., Wake D. A., Smail I., Best P. N., Baugh C. M., Stott J. P., 2012, MNRAS, 426, 679
Gilbank D. G. et al., 2010, MNRAS, 405, 2419
Graham A., Lauer T. R., Colless M., Postman M., 1996, ApJ, 465, 534
Grogin N. A. et al., 2011, ApJS, 197, 35
Hopkins P. F., Hernquist L., Cox T. J., Di Matteo T., Robertson B., Springel V., 2006, ApJS, 163, 1
Hopkins P. F. et al., 2010, ApJ, 724, 915
Huertas-Company M., Rouan D., Tasca L., Soucail G., Le Fèvre O., 2008, A&A, 478, 971
Ichikawa T., Kajisawa M., Akhlaghi M., 2012, MNRAS, 422, 1014
Kanwar A., Simard L., Schade D., Gwyn S. D. J., 2008, ApJ, 682, 907
Kartaltepe J. S. et al., 2012, ApJ, 757, 23
Kaviraj S. et al., 2012, MNRAS, in press
Kennicutt R. C. Jr, 1998, ARA&A, 36, 189
Kereš D., Katz N., Weinberg D. H., Davé R., 2005, MNRAS, 363, 2
Koekemoer A. M. et al., 2011, Astrophys. J. Suppl., 197, 36
Lacey C., Cole S., 1993, MNRAS, 262, 627
Lawrence A. et al., 2007, MNRAS, 379, 1599
Le Fèvre O. et al., 2000, MNRAS, 311, 565
Lilly S. J., Le Fevre O., Hammer F., Crampton D., 1996, ApJ, 460, L1
Lin L. et al., 2008, ApJ, 681, 232
López-Sanjuan C., Balcells M., Pérez-González P. G., Barro G., García-Dabó C. E., Gallego J., Zamorano J., 2009, A&A, 501, 505
Lotz J. M., Primack J., Madau P., 2004, AJ, 128, 163
Lotz J. M., Madau P., Giavalisco M., Primack J., Ferguson H. C., 2006, ApJ, 636, 592
Lotz J. M. et al., 2008, ApJ, 672, 177
Lotz J. M., Jonsson P., Cox T. J., Primack J. R., 2010, MNRAS, 404, 575
Lotz J. M., Jonsson P., Cox T. J., Croton D., Primack J. R., Somerville R. S., Stewart K., 2011, ApJ, 742, 103
Ly C., Lee J. C., Dale D. A., Momcheva I., Salim S., Staudaher S., Moore C. A., Finn R., 2011, ApJ, 726, 109
Madau P., Ferguson H. C., Dickinson M. E., Giavalisco M., Steidel C. C., Fruchter A., 1996, MNRAS, 283, 1388
Mosleh M., Williams R. J., Franx M., Kriek M., 2011, ApJ, 727, 5
Peng C. Y., Ho L. C., Impey C. D., Rix H.-W., 2002, AJ, 124, 266
Pozzetti L. et al., 2010, A&A, 523, A13
Reddy N. A., Steidel C. C., 2009, ApJ, 692, 778
Reddy N. et al., 2012, ApJ, 744, 154
Rodighiero G. et al., 2010, A&A, 518, L25
Rodighiero G. et al., 2011, ApJ, 739, L40
Sargent M. T., Béthermin M., Daddi E., Elbaz D., 2012, ApJ, 747, L31
Scarlata C. et al., 2007, ApJS, 172, 406
Scoville N. et al., 2007, ApJS, 172, 1
Sérsic J. L., ed, 1968, Atlas de Galaxias Australes, Observatorio Astronomico, Cordoba, Argentina
Shapiro K. L. et al., 2008, ApJ, 682, 231
Sobral D. et al., 2009, MNRAS, 398, 75
Sobral D., Best P. N., Geach J. E., Smail I., Cirasuolo M., Garn T., Dalton G. B., Kurk J., 2010, MNRAS, 404, 1551
Sobral D., Best P. N., Smail I., Geach J. E., Cirasuolo M., Garn T., Dalton G. B., 2011, MNRAS, 411, 675
Sobral D., Best P. N., Matsuda Y., Smail I., Geach J. E., Cirasuolo M., 2012, MNRAS, 420, 1926
Sobral D., Smail I., Best P. N., Geach J. E., Matsuda Y., Stott J. P., Cirasuolo M., Kurk J., 2013, MNRAS, 428, 1128
Somerville R. S., Primack J. R., Faber S. M., 2001, MNRAS, 320, 504
Somerville R. S., Hopkins P. F., Cox T. J., Robertson B. E., Hernquist L., 2008, MNRAS, 391, 481
Springel V. et al., 2005, Nat, 435, 629
Swinbank A. M. et al., 2010a, MNRAS, 405, 234
Swinbank A. M. et al., 2010b, Nat, 464, 733
Swinbank A. M., Sobral D., Smail I., Geach J. E., Best P. N., McCarthy I. G., Crain R. A., Theuns T., 2012, MNRAS, 426, 935
Tacconi L. J. et al., 2010, Nat, 463, 781
Trujillo I., Conselice C. J., Bundy K., Cooper M. C., Eisenhardt P., Ellis R. S., 2007, MNRAS, 382, 109
Villar V., Gallego J., Pérez-González P. G., Pascual S., Noeske K., Koo D. C., Barro G., Zamorano J., 2008, ApJ, 677, 169
Wang T. et al., 2012, ApJ, 752, 134
Wardlow J. L. et al., 2011, MNRAS, 415, 1479
Williams R. J., Quadri R. F., Franx M., van Dokkum P., Labbé I., 2009, ApJ, 691, 1879

APPENDIX A: M_{20} SIMULATIONS

We discuss here the effect of the SExtractor property DEBLEND_MINCONT on the segmentation map and derived M_{20} value. In Section 3.2.1, we find that by analysing the M_{20} values and visual classification of a sample of $z = 1.4$–2.5 star-forming galaxies, a segmentation map generated with a value of DEBLEND_MINCONT=0.1 provides a demarcation between major mergers and non-mergers, with a boundary found at $M_{20} \sim -1.5$ (we later fix this value to -1.45).

To quantify how the M_{20} value relates to a major merger we run some very basic simulations. The simulations comprise of moving one artificial galaxy towards another and plotting the variation of M_{20} with distance. The artificial observations are created using the GALFIT software with both galaxies being face-on discs (i.e. Sérsic index, $n = 1$) of the same magnitude and half-light radius. We first perform an analysis appropriate to the high-redshift star-forming galaxies for which DEBLEND_MINCONT=0.1 is found to efficiently select mergers. For the simulations, we use the appropriate values of the sky noise, magnitude zero-point and PSF of the observation we are simulating. The results of this simulation are presented as the black points in Fig. A1. This demonstrates that for a DEBLEND_MINCONT=0.1 and CANDELS *HST* data the M_{20} value

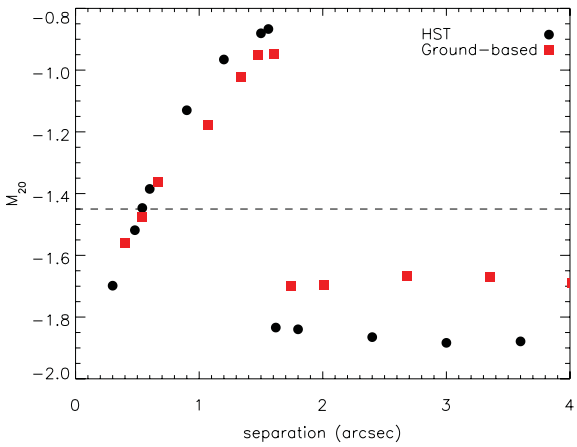

Figure A1. The M_{20} value plotted against separation derived from a simple simulation of two identical face-on disc galaxies approaching each other, as described in the text. The simulated ground-based data are represented by red squares and the simulated *HST* data are black circles. To make the separations at which the M_{20} value jumps to be the same, we adopt a DEBLEND_MINCONT=0.10 and 0.03 for the creation of the space- and ground-based SExtractor segmentation maps, respectively. The horizontal line at $M_{20} = -1.45$ represents the boundary between mergers above and non-merger below which we adopt throughout the paper.

remains low and consistent with being a non-merger for galaxy separations down to ∼1.6 arcsec (∼13 kpc at $z = 0.84$–2.23), as the galaxies have individual segmentation maps. Once this separation drops below this value the two galaxies share the same segmentation map and thus the M_{20} value jumps dramatically as the top 20 per cent of the light is now spread over two locations rather than one. As the separation decreases further, this value lowers until a point is reached where the top 20 per cent of the light is essentially colocated at the centre of a single bright galaxy and as such the M_{20} curve resembles a 'shark fin'. The distance over which this system would be classed as a merger is then ∼1 arcsec which at $z = 0.84$–2.23 corresponds to a distance of ∼8 kpc.

Potentially, the most important factor influencing the M_{20} value for a given galaxy is whether it is derived from the space-based *HST* data as discussed above or from the ground-based imaging with a significantly larger PSF and different background characteristics. We first investigate this by using the original space-based value of DEBLEND_MINCONT=0.1 on the ground-based data and find that this gives a factor of ∼2 larger range in separation over which the galaxies would be classified as a merger and would thus result in an increase in merger numbers relative to the *HST* imaging. A value of DEBLEND_MINCONT=0.03 accounts for this difference, equalling the separation over which a 'merger' occurs with the results plotted as red squares in Fig. A1. This plot confirms the slope in the relation seen between ground- and space-based derived M_{20} seen in Fig. 5 and used to calibrate the ground-based values.

For the lower redshift $z = 0.4$ sample, this angular distance range corresponds to 5.3 kpc and as such may miss some galaxies that would have been classed as mergers in the higher z samples. We therefore alter the value of DEBLEND_MINCONT to 0.11 for the CANDELS and 0.04 for ground-based imaging to account for this so that the same separation in kiloparsec is used at each redshift.

By varying the relative magnitudes of the galaxies and assuming that the flux is linearly proportional to the mass and the size is proportional to the square root of the mass we test what mass ratio of mergers can be seen with this method. The result is that the M_{20} coefficient is sensitive to mergers with a luminosity (mass) ratio down to ∼1 : 10 (in agreement with the simulations of Lotz et al. 2010). For mass ratios less than this the M_{20} coefficient does not increase significantly when the two galaxies share the same segmentation map.

This paper has been typeset from a TEX/LATEX file prepared by the author.